JOURNAL OF MATERIALS SCIENCE 25 (1990) 4361–4376

Fracture mechanism maps for advanced structural ceramics

Part 1 *Methodology and hot-pressed silicon nitride results*

G. D. QUINN
US Army Materials Technology Laboratory, Watertown, Massachusetts 02172, USA

The static fatigue behaviour of advanced structural ceramics can be controlled by a variety of failure mechanisms. A fracture mechanism map can define the stress–temperature regimes where the different mechanisms are dominant. The static fatigue resistance of a hot-pressed silicon nitride with magnesia sintering aid is limited by slow crack growth or creep fracture depending upon the specific stress–temperature conditions. The flexural fracture map is considerably refined relative to earlier versions, and in conjunction with available tension data, was used to create a tension fracture map. The fracture map brings together the findings of a number of studies and can be appreciated by materials scientists and engineers.

1. Introduction

Static fatigue and stress rupture studies for advanced structural ceramics have often examined one mechanism of time-dependent failure. In the 1970s work was focused on slow crack growth (SCG) from pre-existing flaws in silicon nitrides and carbides. These flaws limit the fast fracture strength and are typically inclusions, pores, machining damage, or even artificially implanted Knoop defects. A review paper and bibliography of such work has been published previously [1].

More recent studies have been concerned with creep crack growth or creep fracture. Under certain stress–temperature conditions, creep deformations can blunt pre-existing defects. Excessive creep deformation may however, lead to microcrack nucleation, intergranular growth, and coalescence leading to fracture. Although both SCG and creep fracture mechanisms have intergranular crack growth stages, the key distinction is that slow crack growth emanates from pre-existing flaws, with creep deformations and microcracking confined to the crack tip. Creep fracture on the other hand, has bulk deformation and microcracking and may not necessarily involve pre-existing flaws. Alumina is often used in these more recent studies because of its lower cost and its suitability as a model material [2–7].

Alternative static fatigue mechanisms can be operative in advanced ceramics such as stress corrosion or surface pitting. A convenient scheme to identify the stress–temperature regimes where the respective static fatigue mechanisms are dominant is the fracture mechanism map as first suggested by Wray [8] for a stainless steel. Fracture maps were further developed by Fields *et al.* [9]. Gandhi and Ashby [10] applied the approach to a range of ceramics including several speculative maps for advanced structural ceramics that were available in the early 1970s.

This report presents stress rupture results and a fracture map for a hot-pressed silicon nitride (HPSN). Part 2 [11] applies the approach to a more modern sintered silicon nitride. Preliminary work on the HPSN culminated in empirical procedures to generate a fracture mechanism map [12–14].

2. Material

Hot-pressed silicon nitride (HPSN), grade NC 132 (Norton Co., Worcester, Massachusetts), was fabricated with a magnesia sintering aid and has been characterized previously [14–18]. Principle contaminants were determined by emission spectroscopy to be aluminium (0.28 wt %), cobalt (0.17%), iron (0.32%) and titanium (0.12%). Tungsten was also detected at the level of several per cent but some of this was pick-up from the pulverizing apparatus. All results herein were obtained with specimens from two 150 mm × 150 mm × 25 mm billets (A and P) which had consistent static fatigue behaviour. Flexure specimens were either 2.1 mm × 2.8 mm × 51 mm (as-machined experiments) or 2.3 mm × 3.6 mm × 51 mm (artificial flaw experiments). In all, 550 specimens were prepared.

3. Experimental procedure

All experiments were performed in four-point flexure. While it is generally agreed that direct tension testing is to be preferred, such testing capability was not available for this programme. Indeed, the high number of specimens required to develop a fracture map, and the very long duration of the experiments often necessary (> 1 y) mitigate against direct tension testing. The state-of-the-art of ceramics testing is evolving at the present time, and future studies based upon complimentary flexure and direct tension testing will become more common.

The room-temperature fast fracture strength was evaluated to serve as a baseline strength and to identify the typical strength-limiting flaws. Four-point fixtures with fixed loading pins and 30.5 mm × 15.2 mm spans and a 0.5 mm min^{-1} cross-head rate were used. All testing was in air with ambient humidity and temperature levels.

Elevated temperature flexure was performed with hot-pressed silicon carbide fixtures with spans of either 19 mm × 38 mm or 20 mm × 40 mm. Load bearings were fixed. (Preliminary experiments with rolling bearing high-temperature fixtures have had partial success, but were not used for this study. The rolling action is necessary to eliminate unwanted friction constraints in the specimen which cause an error in stress.) All stress rupture experiments were done with dead weight loading applied into 15 test furnaces described previously [18, 19]. The individual furnaces were all consistent within 5° C. Errors in stress due to the loading system were kept to less than 2%. The furnaces were allowed to sit at temperature for 5 min prior to loading to let the furnace stabilize. Loading was done manually by lowering a laboratory jack such that the weights were transmitted on to the loading lever in 5 sec. Elapsed time was measured from the instant full load was applied, and failure time was noted by a timer on each furnace. The instant a specimen failed, the furnace power was automatically shut off so that primary fracture surfaces could be preserved.

Stress rupture data in this paper are represented on log time axes that being at 0.001 h (3.6 sec). The exact manner of loading surely will affect experiments of such duration and make them less accurate than longer experiments. Applied stresses were computed on the basis of the elastic beam formula for the maximum tensile stress on the tensile surface. Nearly all origins of failure were from this region. In many instances large cracks grew and extended into the bulk. This would surely alter the stress state, but it can be demonstrated using any one of the crack growth formulations that the crack size is small over the major portion of the lifetime of the specimen. Creep relaxations were present in many of the specimens, in which case the elastic formulation for stress was an overestimate.

The state of stress in a flexure specimen is a strong function of time and temperature if creep occurs. A number of authors have attempted to analytically correct or adjust their results to correct for creep relaxations, but such work has been hampered by the number of assumptions involved, particularly in the choice of constitutive equations. Primary creep can be significant [20–24], the secondary creep rate is often nonlinear with time [21, 25], rates in tension and compression are significantly different [20, 23, 26], viscoelasticity can be present [25], and devitrification [2, 27] and chemical gradients from oxidation through the specimen thickness [28, 29] are complicating factors. Creep microcracking will alter the specimen compliance [30], and accumulated tension damage can distort the measured creep exponents [30, 31]. The secondary creep rate is often not achieved in hundreds or even thousands of hours [25, 32]. Several of these phenomena are well illustrated for a siliconized silicon carbide [33], wherein it was shown that the neutral axis of the flexure specimen had migrated drastically. These phenomena are often very significant and will cause great variability in the constitutive equations through the thickness of the specimen, especially if more than one phenomenon is operative. Another good example is from Wiederhorn *et al.* [2], wherein a myriad of constitutive equations become pertinent in an aluminium oxide with a glass boundary phase that devitrified at different rates from the compression to the tension side. In such cases, Wilkinson [27] concluded that it is "virtually impossible to extract meaningful creep data from tests performed in bending". Attempting to model flexural creep with simplified constitutive equations and then adjusting parameters to get a best fit to the data is a curve-fitting exercise. Jakus and Wiederhorn [32] point out that erroneous creep exponents can be an artefact of flexure testing. Furthermore, frictional constraints of fixed knife edges and contact point tangency shifts of specimens that have crept more than a few tenths of per cent strain have been completely ignored. Therefore, it must be concluded that in many instances, detailed analyses of flexural creep data are not warranted.

All stresses in this study were left in terms of the applied elastic stresses which are certainly correct for specimens with no creep, and for short times even if there is creep. Clearly, direct tension and compression testing are preferred for future studies. Jakus and Wiederhorn [32] have reached the same conclusion.

Creep deformations were not measured during the experiments, but final deformations were used to compute an apparent strain-at-failure, ε_f, from the formula

$$\varepsilon_f = 4tv/L^2 \qquad (1)$$

where t is specimen thickness, v is the midspan deflection relative to the inner load pins, and L is the outer span length. Even this formula is an oversimplification, because it assumes the strains in compression and tension are equal.

Specimens were tested in either the as-machined state or with an implanted artificial flaw. In the latter case, a Knoop indentation was made on a polished surface, which created not only the hardness impression, but a subsurface semi-elliptical crack as depicted in Fig. 1. The purpose was to create a flaw large enough to guarantee it was the severest in the specimen and to control precisely its size and location. No provision was made to remove the residual indentation stresses because it was originally assumed they would be annealed during furnace heating (an unavoidable step) or during the customary 5 min soak prior to load application. An indentation load of 15.7 N was used on 240 HPSN specimens reported in this paper. (Experiments with alternative loads have been reported earlier [17].) This load created a semi-elliptical surface flaw of 50 μm depth which limited the room-temperature strength to 370 MPa. Such artificial flaws were more severe than the natural defects which limited strength to 500 to 1000 MPa.

4. Results

The average flexure strength of 16 specimens from billet A was 909 MPa with a 67 MPa standard deviation. The Weibull two-parameter modulus (m) from

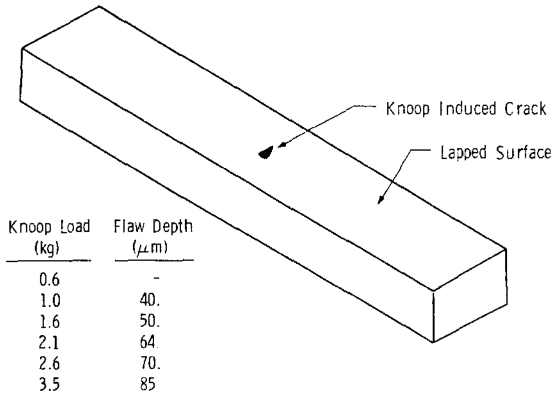

Knoop Load (kg)	Flaw Depth (μm)
0.6	-
1.0	40.
1.6	50.
2.1	64
2.6	70.
3.5	85

Figure 1 Flexure specimen with an artificially implanted semi-elliptical surface defect. The flaw depth for HPSN varies with the Knoop indentation load. A load of 15.7 N (1.6 kg) was used for the specimens in this study.

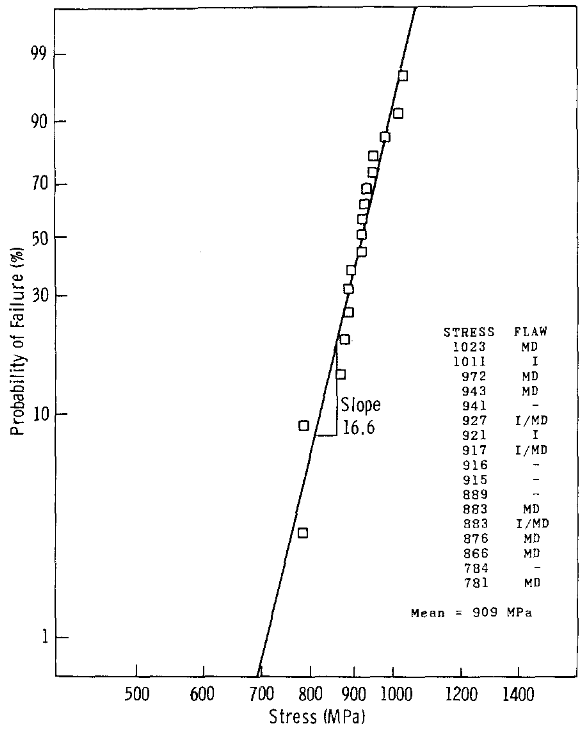

STRESS	FLAW
1023	MD
1011	I
972	MD
943	MD
941	-
927	I/MD
921	I
917	I/MD
916	-
915	-
889	-
883	MD
883	I/MD
876	MD
866	MD
784	-
781	MD

Mean = 909 MPa

Figure 2 Room-temperature flexure strength of the as-machined HPSN specimens. The insert lists the individual strength data and the strength-limiting flaw. MD, machining damage; I, inclusion; I/MD, an inclusion or machining damage; (–) uncertain.

a least squares analysis was 16.6 (Fig. 2). Machining damage was the most common strength-limiting defect (~ 20 μm deep), with some tungsten carbide or silicide inclusions as well, as shown in the labelled Weibull plot, Fig. 2. Ten specimens from billet P (which was prepared from the same powder lot) had a mean strength of 872 MPa, a 54 MPa standard deviation, an m of 19.1, and identical strength-limiting defects. The flexure strength of specimens from the two billets are thus quite consistent. The combined mean strength is 895 MPa and the Weibull modulus is 17.2 and the characteristic strength of the bend specimen is 923 MPa. The characteristic strength for a volume of 1 mm^3 would be 988 MPa. Subsequent stress rupture testing confirmed that the static fatigue behaviour of the two billets was also identical.

Fig. 3 presents the stress rupture outcomes for the as-machined HPSN specimens. The scatter in time-to-failure is remarkably small over the 1100 to 1400° C range. Points with arrows are either specimens that failed on loading, or specimens which survived intact. A power law relationship exists between crack velocity (v) and stress intensity (K_I) [34, 35]

$$v = AK_I^N \exp(-Q_{scg}/RT) \qquad (2)$$

where N and A are constants, Q_{scg} is the activation energy of slow crack growth, R is the gas constant, and T is the absolute temperature. It can be shown that the stress rupture data should be linear on a log stress–log time graph as shown in Fig. 3 [36, 37]. The inverse negative slope of the stress rupture curves is the slow crack growth exponent, N. The values of N from Fig. 3 are 29.6, 19.5, 12.8, 9.9, and 9.2 for 1000, 1100, 1200, 1300, and 1400° C, respectively. These exponents are upper limits because the elastic stresses are overestimates for the longer duration experiments because of creep relaxation of the stress.

The results also plot very well on a semilog format of stress against log time as discussed in [14]. From 1100 to 1400° C, the data are well represented by the relationship

$$t_f = 3.09 \times 10^{-21} \exp(180/RT) \exp(-0.037\sigma_a) \qquad (3)$$

where t_f is the time-to-failure (h) and σ_a is the applied elastic stress (MPa). The apparent activation energy is 180 kcal mol^{-1}.

The remarkable reproducibility of stress rupture results for this particular grade HPSN is illustrated in

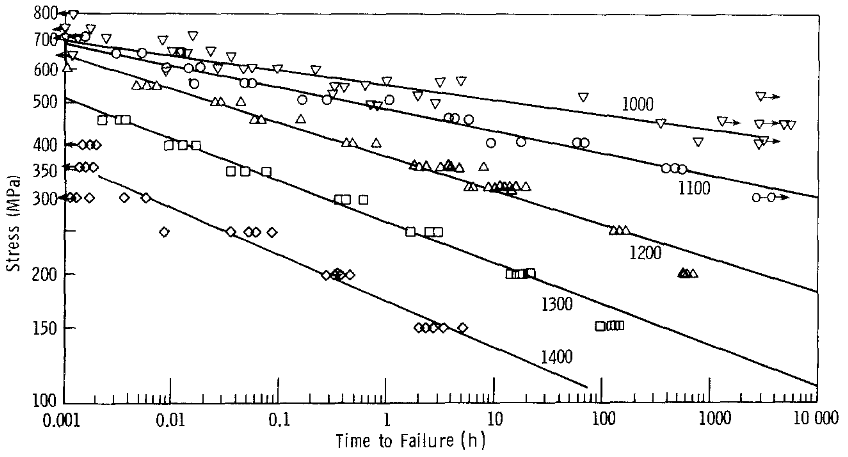

Figure 3 Flexural stress rupture results from as-machined HPSN. Temperatures were from 1000 to 1400° C as shown. All stresses are elastic stresses.

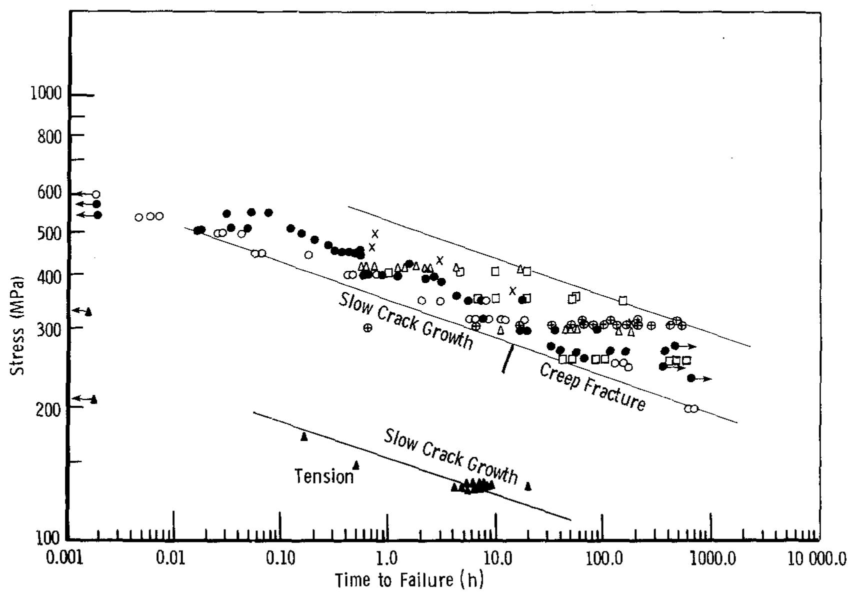

Figure 4 Stress rupture results for HPSN at 1200° C. There is a remarkable consistency in the flexural results. Elastic flexure stresses are shown. The tension results are shifted to lower stresses. (⊕) [38], (×) averages [39], (△) [40, 41], (▲) tensile [40, 41], (○) [13, 14, 17], (●) [18], (□) [42].

Fig. 4. There is excellent agreement among the flexure results despite different source billets, specimen sizes, specimen preparations, test fixtures, and laboratories involved [14, 17, 18, 38–42]. This helps explain why this vintage HPSN has gained wide acceptance as a model structural ceramic. More stress rupture data exist for this material than for any other high-performance ceramic. The variation in median time-to-failure of the different studies is at most a factor of 10 and can be traced to billet to billet differences or variability in the baseline strength. Systematic differences in the baseline strength from billet to billet are known to exist in this material [17, 43–48]. The variability in absolute times to failure is probably related to the precise MgO/SiO_2 molar ratio of the starting powders [45]. The fatigue-resistance parameters are nontheless very consistent [17, 38, 49].

Fig. 5 is an alternative representation of the same stress rupture data. In this instance, the graph has axes of stress and temperature and the loci are for constant failure times. These loci were interpolated from graphs such as Fig. 3. The reason for presenting the data in this format will be evident shortly.

Fig. 6 shows the results for 162 specimens with the artificially implanted, 50 μm deep flaws. The fast fracture strength is 370 MPa and is marked with a bar. Each labelled point in the figure corresponds to a stress temperature condition at which stress rupture experiments were conducted. The points are labelled by a ratio which gives the number of specimens that did fail from the artifical flaw, to the total number tested. The number in parentheses is the geometric mean time to failure. For example, at 266 MPa and 1200° C, of seven specimens tested, six broke at the flaw and the geometric mean time to failure was 60 h.

Fig. 7 shows fracture surfaces with obvious SCG from the artificial flaw. The intergranular SCG zone relative to the transgranular artificial flaw and subsequent fast fracture zones makes fractographic interpretation quite easy, another reason why this material is suitable as a model ceramic. Severe oxidation and surface pitting can occur during the experiments as shown in Fig. 7b. This undoubtedly reduces the strength, yet this degradation mechanism never did "catch up" with the SCG or creep fracture mechanisms. (There is one instance where a surface pit did cause a time-dependent failure. This was a tension specimen tested by Govila [40, 41] at 1204° C at 133 MPa which failed at the atypical time of 21 h. This probably was due to an excessive surface oxide reaction due to contaminants from strain gauge burn-off.)

Of special interest are four experiments of extreme duration. Three were at 1100° C and 266 MPa (Fig. 6). Only two specimens were tested to failure, at 17 376 and 14 941 h. (Failure occurred in the gauge length and not at the load pins on these.) The former broke from the artificial flaw but with 1.9% strain. The latter failed such that the fracture surface had several tiers, including one with the artificial flaw on it, probably by coincidence. This specimen certainly failed due to creep fracture and had a final strain of 1.7%. The third experiment was regretably terminated at 10 000 h while the specimen was still intact due to an equipment problem. The final extreme duration experiment was at 1150° C and 200 MPa with failure occurring at 9 100 h, but not from the artificial flaw. Fig. 8 shows a specimen that failed from creep fracture. Tighe [46] showed similar extreme creep cracking. Creep fracture typically is more severe at a surface [47] presumably due to the lower constraint relative to an internal crack. Similarly, edge creep cracking will often be more severe as shown in Fig. 8b.

In one instance where a large number (19) of experiments were performed at the same condition (266 MPa, 1250° C), the log of time-to-failure was normally distributed. The geometric mean and the median thus coincide. The geometric mean was 5.7 h and the standard deviation was 0.13.

5. Discussion

Over much of the field in Fig. 6, failure did occur as the result of SCG from the artificial flaws. Alternatively, at lower stresses, there is a distinct regime where creep fracture was dominant because creep deformation was significant and specimens did not fail from the dominant original flaws. Instead fracture was controlled by creep fracture. Excessive creep plasticity blunted the initial defects, restricting their growth.

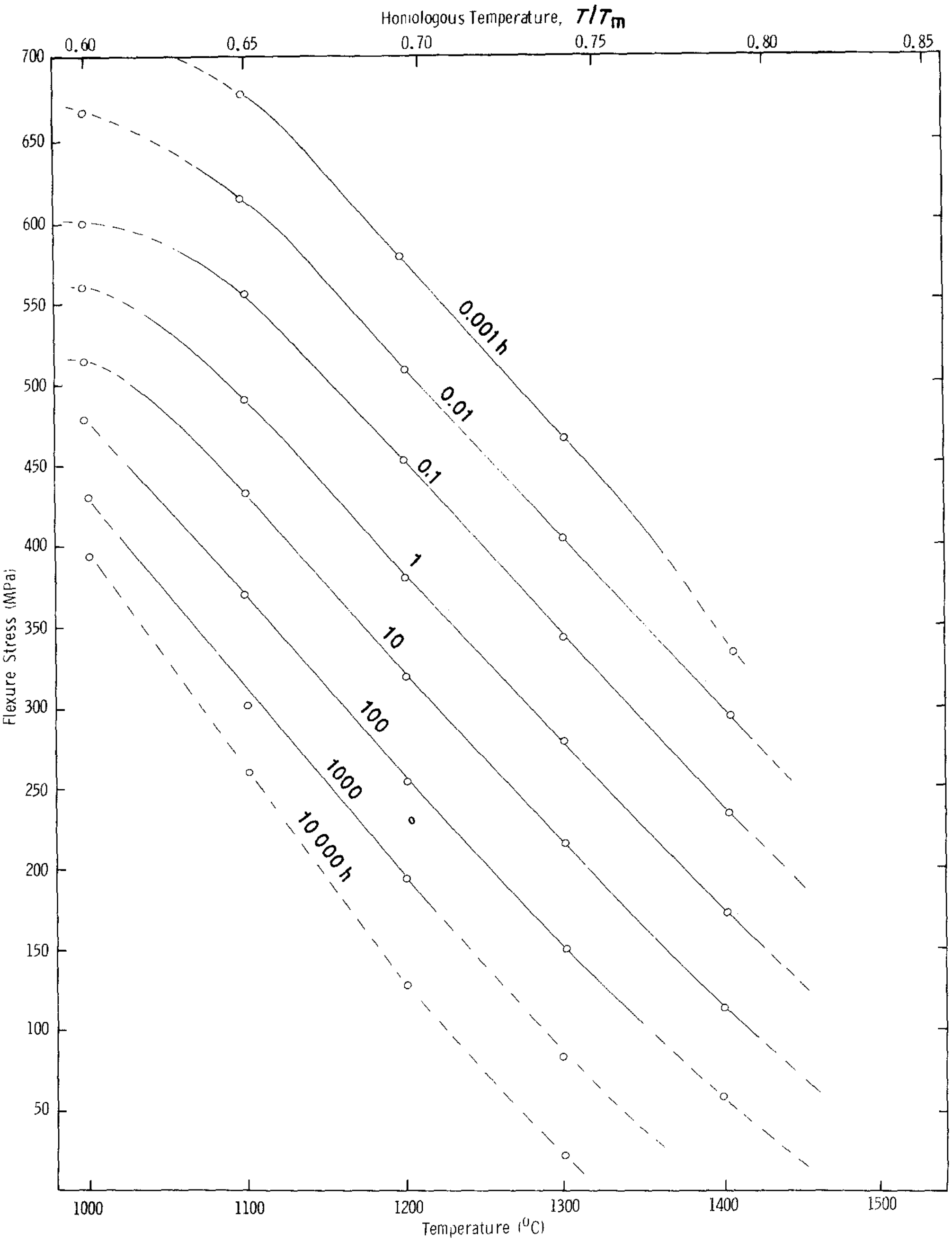

Figure 5 Flexural stress rupture results for as-machined HPSN specimens. This is an alternative representation of the results of Fig. 3.

Ultimately, however, the high deformation leads to extensive microcrack nucleation, growth, interaction and ultimately rupture. This is one of the principle findings of this work: that fractographic analysis is capable of discerning the conditions wherein either slow crack growth or alternatively creep fracture mechanisms are dominant.

Das *et al.* [28] have supportative findings in that five flexure specimens at 1300° C and 196 MPa did not break from 2.6 kg Knoop flaws implanted in them. This is not surprising, because the conditions are close to the creep fracture regime in Fig. 6. Times-to-failure were appreciably shorter than in the present study, but the latter study was in vacuum. Kossowsky *et al.* [47] also show a substantial decrease in stress rupture lifetime and strain in inert atmospheres relative to air for HPSN.

The SCG–creep fracture regimes are further defined by comparing the loci of failure time of the artificially flawed compared to the as-machined specimens as shown in Fig. 9. Over much of the field, slow crack growth from pre-existing flaws did lead to fracture. The artificially flawed specimens (solid lines) failed in less time than similarly loaded as-machined specimens (dotted lines) because there was less crack growth necessary to reach a critical condition. In sharp contrast, however, the failure loci coincide under some conditions, which means the artificial flaws had no effect whatsoever upon the failure time. This is the creep fracture regime.

Total apparent strains in the creep fracture regime were of the order of 1% or more and there was no clear correlation of the creep fracture–SCG boundary with per cent deformation as shown in Fig. 10. The apparent strain is an underestimate, however, because the neutral axis migrates into what once was the compression half of the specimen [32].

The shaded boundary which separates the SCG and creep fracture regimes levels off at about 260 MPa. This level is influenced by the size of the initial

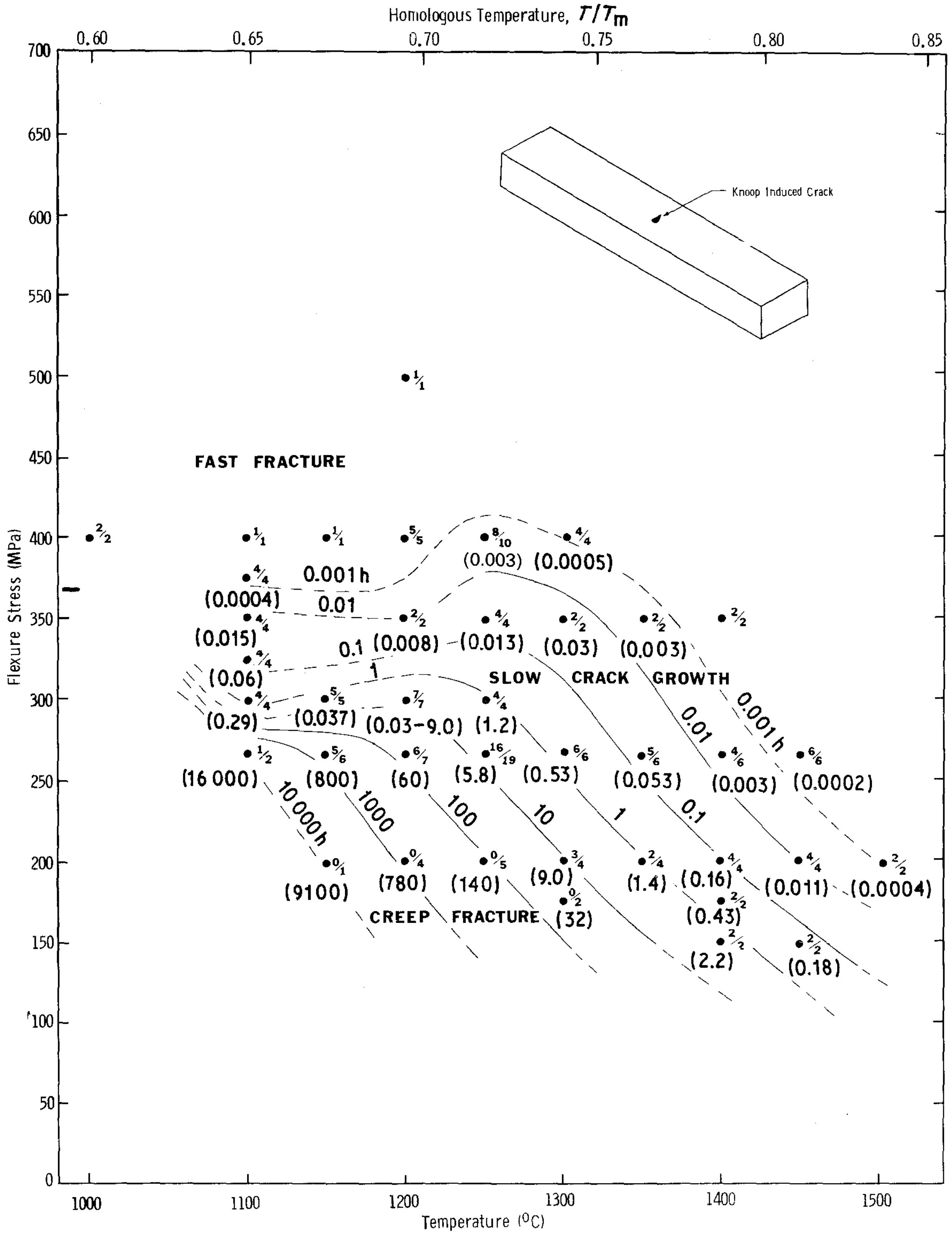

Figure 6 Flexural stress rupture results for artificially flawed HPSN specimens. Each dot is a stress–temperature combination where experiments were performed. The dot is labelled by a ratio which gives the number of specimens that broke from the artificial flaw relative to the total number of specimens tested. The geometric mean time-to-failure is given in parentheses. Loci of constant failure time in (h) are shown. In the creep fracture regime, none of the specimens failed from the artificial flaw.

artificial flaws [14]. The larger the initial flaws, the more likely SCG will cause fracture, and the boundary can be shifted downward somewhat.

The apparent activation energies for the two mechanisms can be assessed in Fig. 11. Artificially flawed specimens loaded at 200 or 266 MPa encompass both the creep fracture and SCG regimes. There is no significant change in slope in either line, implying the same activation energy applies to both mechanisms. The apparent energies are 211 and 216 kcal mol^{-1} which is is reasonable agreement with the 180 kcal mol^{-1} estimated from the natural flaw experiments (Equation 3). This is the activation energy for a grain-boundary sliding processes involving the viscous grain-boundary phase which accounts for both SCG and creep. Transmission electron microscopy studies of HPSN stress rupture specimens have confirmed that this mechanism is responsible for creep deformation, creep fracture and slow crack growth [46–48, 50]. Mosher *et al.* [51] reported an activation energy for viscous flow of the grain boundary phase of 166 kcal mol^{-1} in HS 130, which is a similar grade HPSN (Norton Co., Worcester, Massachusetts, and Joseph Lucas Co., West Midlands, UK; Torti [15]

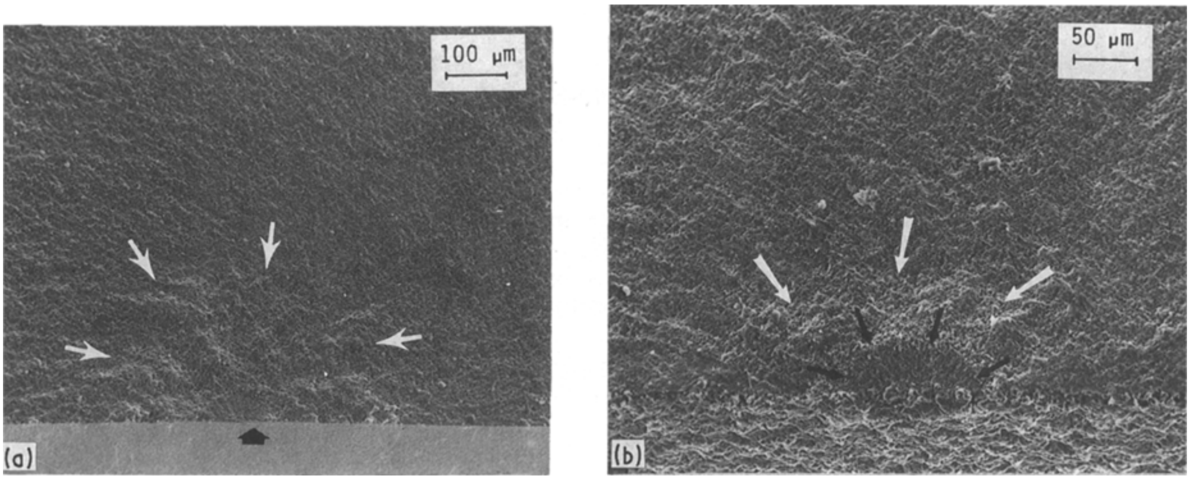

Figure 7 HPSN fracture surfaces illustrating SCG (white arrows) from the Knoop defect (black arrows). (a) Loaded to 400 MPa at 1250° C and failed at 10 sec. (b) Loaded at 175 MPa at 1300° C. The test was interrupted at 210 h and the specimen broken at room temperature. Surface oxidation is much more severe than in (a).

explains the minor difference between HS-130 and NC 132 grades of HPSN). Ud Din and Nicholson [50] found an activation energy of 140 kcal mol^{-1} for flexure specimens tested in creep loading. Kossowsky *et al.* [47] performed direct tension experiments on the same earlier grade HPSN and reported 130 to 150 kcal mol^{-1} but noted that the activation energy increased with increasing purity of the boundary phase. They further noted that lifetime was limited by the creep rate (clearly indicating a creep rupture mode of failure) which is not surprising because their stresses were only 30 to 110 MPa. Nevertheless, they also observed conditions where crack growth from pre-existing flaws (in the SCG regime) led to shorter lifetimes than from creep fracture. Seltzer [52] reported 168 kcal mol^{-1} for both the HS 130 and NC 132 grades of HPSN. Arons and Tien [25] noted two activation energies, however: 202 kcal mol^{-1} for the persistent component of creep, and 172 kcal mol^{-1} for the viscoelastic component.

In summary, the SCG–creep fracture regimes could be defined by two methods: a comparision of times-to-failure between artificial and naturally flawed specimens, and by fractographic observations (does a large initial flaw grow to failure?). Further interpretation of certain aspects of these results including the effects of residual stresses, atmospheric effects, preoxidation effects, and the influence of initial flaw size upon the map boundaries, has been given previously [14].

Fig. 12 puts the results into perspective because the entire range of stress–temperature conditions are shown. The fast fracture strength at room temperature is modelled by Weibull statistics [53, 54]. The median (50%) and 10% and 90% failure bands are shown. A gradual weakening of the material occurs to about 900° C [40, 43, 44] but the strength-limiting flaws are probably the same if the tests are done in the fast fracture mode. Flaw healing or new flaw generation can alter the fast fracture strength as shown, even for relatively short exposure times, however [55]. The onset of static fatigue phenomena occurs in the 800 to 900° C range in air, but scatter is high. Above 1000° C, slow crack growth from pre-existing flaws becomes increasingly consistent and it is possible to mark loci of median failure time. Fig. 12 shows the median line (50%) for fast fracture strength splits into loci of median failure time. The creep fracture regime is put into its proper perspective in Fig. 12 where it is

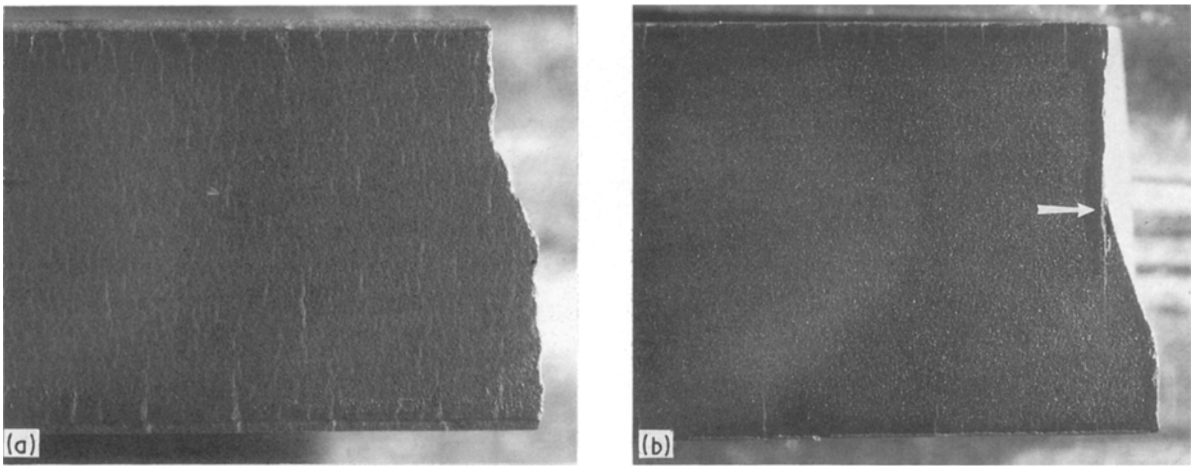

Figure 8 Extreme microcracking on the tensile surface of HPSN specimens that failed in creep fracture. The fracture surface is to the right. (a) A specimen that failed after 1157 h at 1200° C with 200 MPa. The specimen did not fail from the artificial flaw. (b) A specimen which failed after 14 941 h at 1100° C at 266 MPa. The arrow indicates the location of the original artificial flaw.

TABLE I Parameters controlling the strength and life prediction of HPSN

Field	Controlling factors	References	HPSN grade NC 132*
No failure	Stress is too low to cause fracture. Specimens remain intact. For all flaws present, the stress intensity (K_I) is lower than a critical value $K_I < K_{Ic}$ where $K_I = Y\sigma_a\sqrt{c}$ where Y is a shape factor, σ_a is the applied stress, c is the flaw size, K_{Ic} is the critical stress intensity		$K_{Ic} = 4.5$ to $5.0\,\mathrm{MN\,m^{-1.5}}$ [17]
	Specimens can retain the same strength, weaken, or strengthen somewhat, due to flaw healing, blunting, or generation of new flaws.	[55]	
Fast fracture	Stress is too high and causes brittle fracture. For one or more flaws, the stress intensity is too high: $K_I > K_{Ic}$		
Boundary between fast fracture and no failure	Boundary is actually a field due to statistical aspects of the strength of ceramics. Failure is a probabilistic event. Weibull statistics are applicable: Probability of fracture, $P = 1 - \exp - \left[\int^V \left(\frac{\sigma_a - \sigma_u}{\sigma_0}\right)^m \mathrm{d}V\right]$	[53, 54]	
	where m is the Weibull modulus σ_u is the threshold stress, σ_0 is a normalization parameter called the characteristic strength, V is the specimen volume		$m = 17.2$, $\sigma_u = 0$, $\sigma_0 = 988\,\mathrm{MPa}$ for a $1.0\,\mathrm{mm^3}$ effective volume
	Note: uniaxial loading with a single flaw population assumed. The integration can be over the surface if surface flaws predominate.		
Slow crack growth	Fracture is due to slow crack growth of pre-existing flaws. Crack velocity (v) is related to the applied stress intensity: $v = AK_I^N \exp(-Q_{scg}/RT)$	[34, 35]	$Q_{scg} = 180 - 210\,\mathrm{kcal\,mol^{-1}}$
	where Q_{scg} is the activation energy, T is the temperature, N is the slow crack growth exponent, A is a constant.		N at 1000° C = 30 1100° C = 20 1200° C = 13 1300° C = 10 1400° C = 9
	For constant applied stress (stress rupture loading): the crack velocity can be integrated to give the time to failure (t_f): $t_f = [2/(AY^N(n-2))]\sigma_a^{-N}C_i^{(2-N)/2} \exp(Q_{scg}/RT)$	[36, 37]	(N values for this HPSN are surveyed in [17].)
	where c_i is the initial flaw size.		$c_i = 18$ to $30\,\mu\mathrm{m}$ [15] (An alternative expression for t_f is given by Equation 3)
Creep fracture	Fracture is due to the accumulation of excessive creep deformation and damage. This may entail the nucleation, growth and coalescence of microcracks. Given steady state creep where: $\dot{\varepsilon}_{ss} = B\sigma_a^n \exp(-Q_c/RT)$ where $\dot{\varepsilon}_{ss}$ is the steady state strain rate, Q_c is the activation energy for creep, B, n are constants		
	$t_f\dot{\varepsilon}_{ss}^{m^*} = C$	[3, 56]	
	where m^* and C are constants		$m^* = 1.0$, $C = 2.9 \times 10^{-2}$ for t_f in h ([47] HS 130)

*All parameters were evaluated in the present study, unless otherwise noted.

shown as a small field at high temperature and low stress. Finally, the flexural mode of loading, excessive creep leads to the final field where specimens do not fracture, but instead bottom out on the test fixtures. Such a field is not expected for the tensile mode of loading unless superplasticity occurs, but this has not been reported as yet for this material. The failure-controlling or life-prediction parameters for each field are given in Table I.

Deformation maps are well known, but fracture maps are relatively recent. Gandhi and Ashby [10] presented a preliminary diagram for the HS-130 vintage HPSN. Their terminology for the SCG regime was "brittle intergranular fracture 3". They used normalized temperature and stress axes. The temperature axis was homologous temperature which is the absolute temperature normalized by the melting temperature. In the present paper, T_m is set at the decomposition temperature of silicon nitride which is 1850° C [45]. Figs 5, 9, 10 and 12 include such a normalized axis.

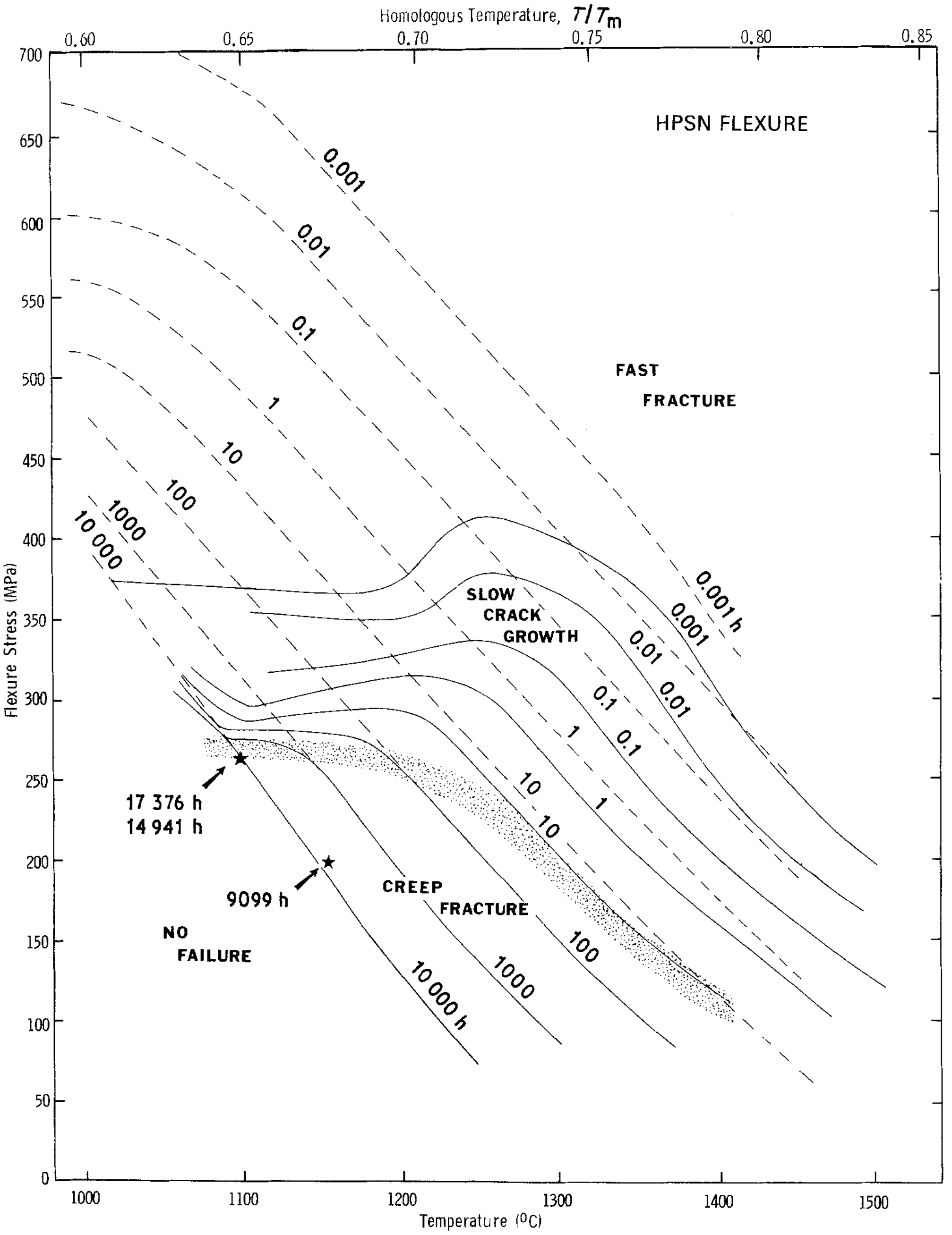

Figure 9 Combined natural (· · ·) and artificial (——) flaw, HPSN stress rupture data. The coincidence of the loci of failure time for both specimen types, determines the creep fracture regime. All stresses are elastic flexure stresses. The stars highlight three unusually long experiments.

(The homologous temperature axes in previous papers [13–16] were in error.) Gandhi and Ashby normalized their stress axis by the elastic modulus, but this ignores differences such as flexure–tension testing, and artificial compared to natural flaws. The fast fracture stress is preferred as a normalization parameter because it takes these factors into consideration.

Grathwohl and his colleagues have also noted the different regimes of slow crack growth and creep fracture in a magnesia-doped HPSN at 1200 and 1300° C [21, 57–59]. Their work included detailed flexural creep strain and oxidation measurements. The transition from SCG to creep fracture was 180 MPa at 1200° C, and 150 MPa at 1300° C in as-machined specimens. These stress levels are similar to those shown in Figs 9 and 12. Grathwohl showed a distinct time lag when the mechanism of failure shifted. (Such time lag was not observed in the HPSN of the present study.) The time lag, and the pattern of the applied stress against time-to-failure plots were directly accounted for by stress relaxation in flexure [21, 59]. Grathwohl further noted that specimens did not fail from artificial flaws in the creep fracture regime, but that very large artificial flaws (multiple 10 kg Knoop indents) tended to extend the creep fracture–SCG boundary to lower stress values, enhancing the SCG regime [59]. Grathwohl's findings and interpretations of the multiple mechanisms of static fatigue failure are in complete accord and are a fascinating complement to the present report.

The fracture map (Fig. 12) is for flexure specimens under constant loading in air. Alternative loading sequences, or pre-oxidizing treatments can have significant effect upon strengths and lifetimes. Oxidation of magnesia-doped HPSN can influence stress rupture performance by creating surface damage or by

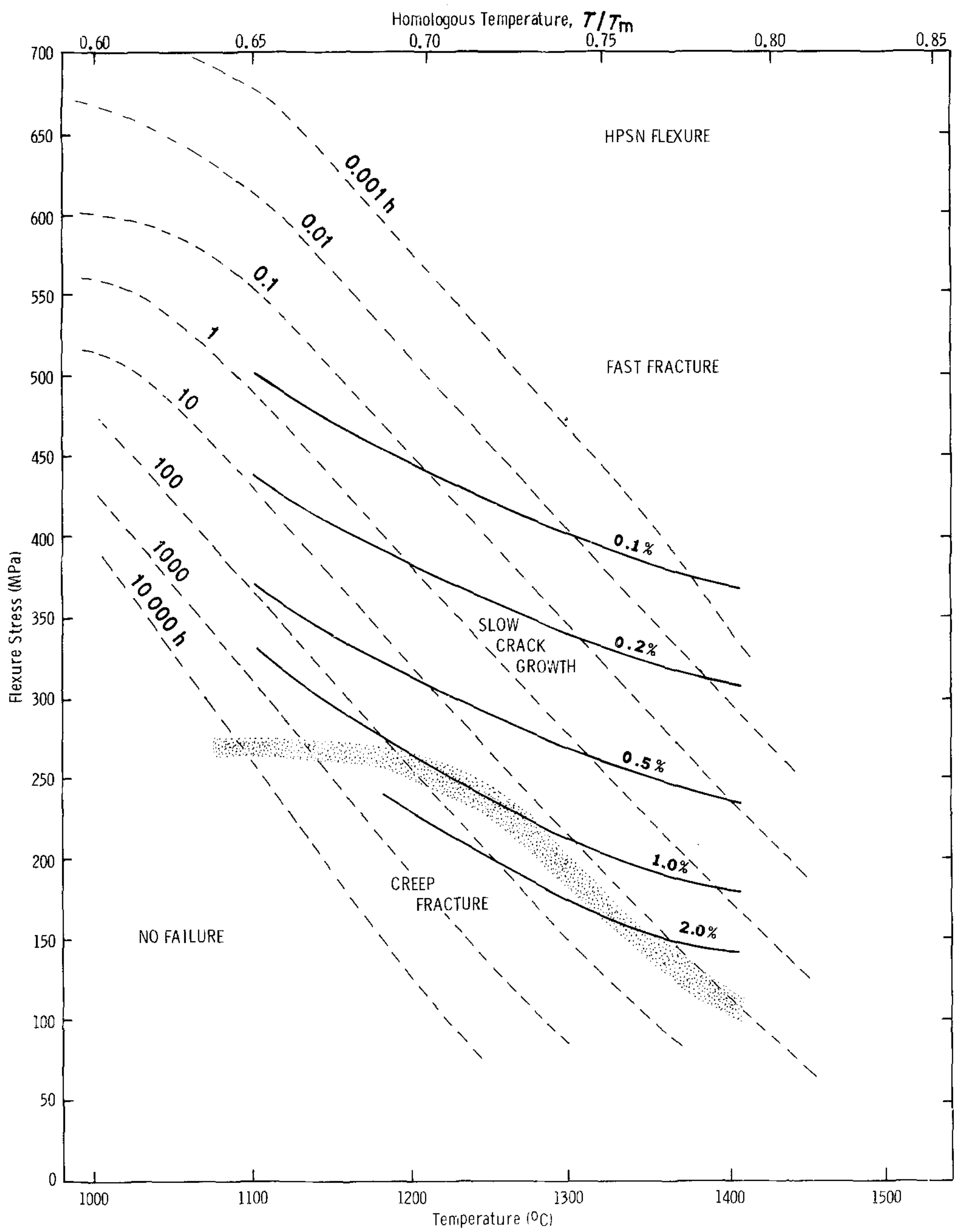

Figure 10 Apparent final creep strains superimposed on the HPSN fracture map.

altering the composition of the second phase at the silicon nitride grain boundaries. This can be either from pre-oxidation treatments, or by oxidation concurrent with a stress rupture experiment. Quinn and Swank [38] showed that a 100 h pre-exposure in air at 1200° C radically decreased static fatigue lifetimes due to the formation of large surface pits from which SCG occurred during subsequent stress rupture testing. This is in contrast to reports of the beneficial effects of such a pre-exposure due to the formation of a surface sink of silica that draws cation impurities or the magnesium additive to the surface, thereby improving the refractoriness of the grain-boundary phase in the bulk [28, 60, 61]. In each of these latter instances, however, it was necessary to remove the oxide layer from the specimen to gain the benefit. The effect of prior exposure upon the fast fracture strength is also considerable [38, 55, 62].

Oxidation of MgO-doped HPSN during the stress rupture experiment can lead to increased creep rates [48, 52] and times-to-failure [48, 52, 58] relative to experiments in inert atmosphere. Grathwohl [59] showed that the oxide layer formed is not oxidation rate limiting in magnesium-doped HPSN and that the creep and slow crack growth resistance of a specimen has a gradient due to the outward diffusion of magnesium to the surface oxide sink. An activation energy of 120 kcal mol^{-1} was measured for this process. Lange *et al.* [61] have demonstrated this compositional gradient. It therefore appears there is an interrelationship between oxidation and the grain-boundary sliding processes that result in creep and slow crack growth phenomena. This can unfortunately complicate life-prediction analysis. For example, there could be a creep or lifetime dependence upon specimen size, related to the diffusion distance for cations to reach the surface. In laboratory flexure specimens, these distances are not significantly different, but real components may be ten times thicker. (Unpublished work by Lenoe [63] demonstrated there may be a size effect upon lifetime in laboratory flexure specimens.)

Multiaxial loadings which might be expected to

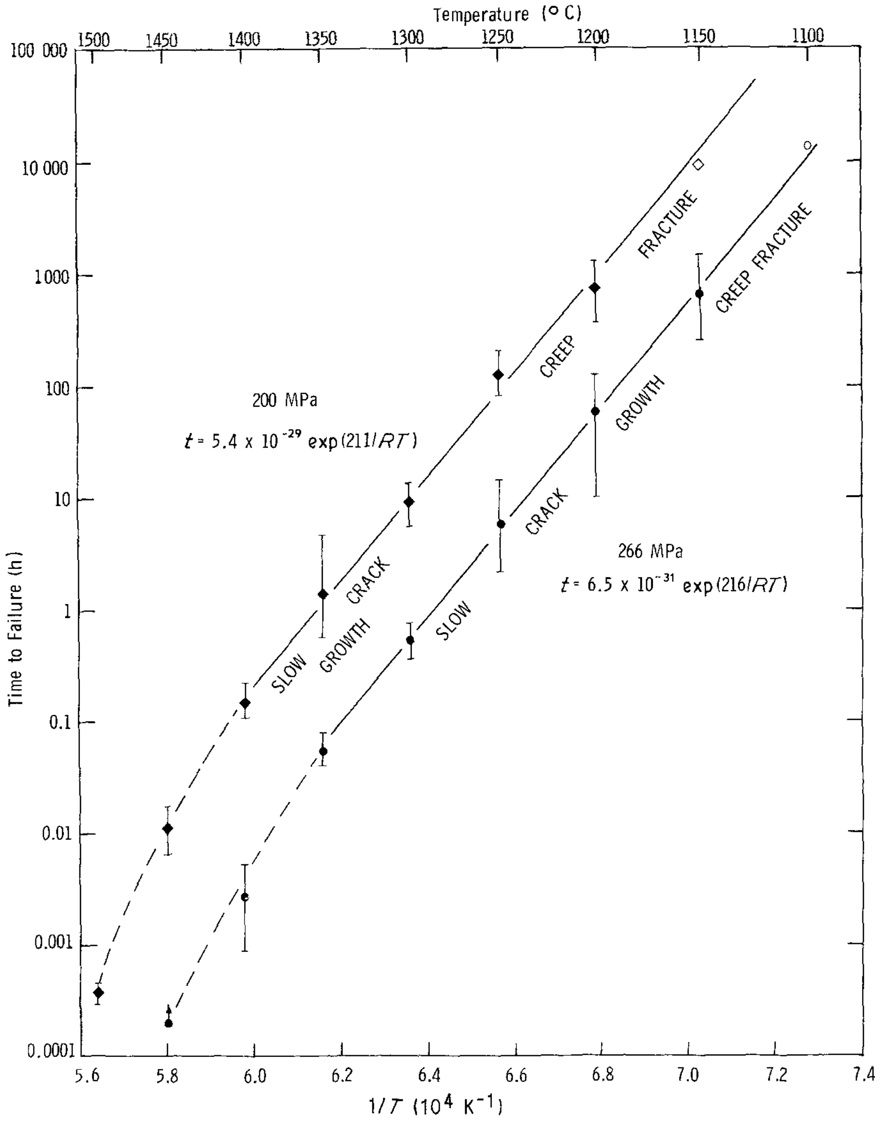

Figure 11 Activation energies for creep fracture and slow crack growth are the same in HPSN. 1.6 kg Knoop flawed.

change the stress rupture lifetimes drastically, have, in fact, not been particularly deleterious in MgO-doped HPSN, providing the reduced fast fracture strength in multiaxial loading is taken into account [64, 65].

5.1. Comparison of tension and flexure results

The utility of the fracture map would be greatly enhanced if it could be generalized to modes of loading other than flexure. Therefore, it is useful to compare the available tensile stress rupture data with flexure data. Govila [40, 41] performed tensile stress rupture tests on this same grade HPSN at 1000, 1204, and 1300° C. Figs 4, 13 and 14 show the results in comparison with flexure data of the present study. The tension results at 1000° C are highly scattered, making comparison difficult. At 1200 and 1300° C the direct tension results are shifted to lower stresses which is not surprising in the light of the Weibull-size effect of strength, and the relaxations in stress to be expected in flexure tests. What is encouraging is that the shifts seem to be by a simple proportional amount in the 0.1 to 100 h range, and this suggests steady state phenomena. Table II gives these proportional shifts*. It was possible from re-examining the detailed fractographs shown by Govila [40] to assess the mechanism of failure in his tensile specimens, and these are noted in Figs 4, 13 and 14. There was only slow crack growth (usually from internal sources) and no creep fracture at 1000 and 1200° C. At 1300° C the fracture surfaces were slow crack growth for specimens with stress over 80 MPa, but at lower stresses crack growth zones were huge (> 50% of the fracture surface) and jagged corresponding to the onset of creep fracture. Thus, there seem to be grounds for assuming the mechanisms of time-dependent failure are the same for the flexure and tension experiments, a fortuitous result.

The dependence of strength upon specimen size is well known and well modelled by Weibull statistics. Davies [54] shows that strength can be correlated between different specimen sizes and modes of loading through the effective volumes (V_E)

$$\frac{\sigma_{\text{flex.}}}{\sigma_{\text{tens.}}} = \left(\frac{V_{\text{E,tens.}}}{V_{\text{E,flex.}}}\right)^{1/m} \quad (4)$$

TABLE II Ratio of flexure to tensile strength at constant failure time for HPSN

Time (h)	1000° C	1200° C	1300° C
1	1.7	2.7	2.7
10	1.6	2.6	2.8

---

*The flexural stress rupture lines were all least squares curve filled, whereas the tension lines were hard drawn.

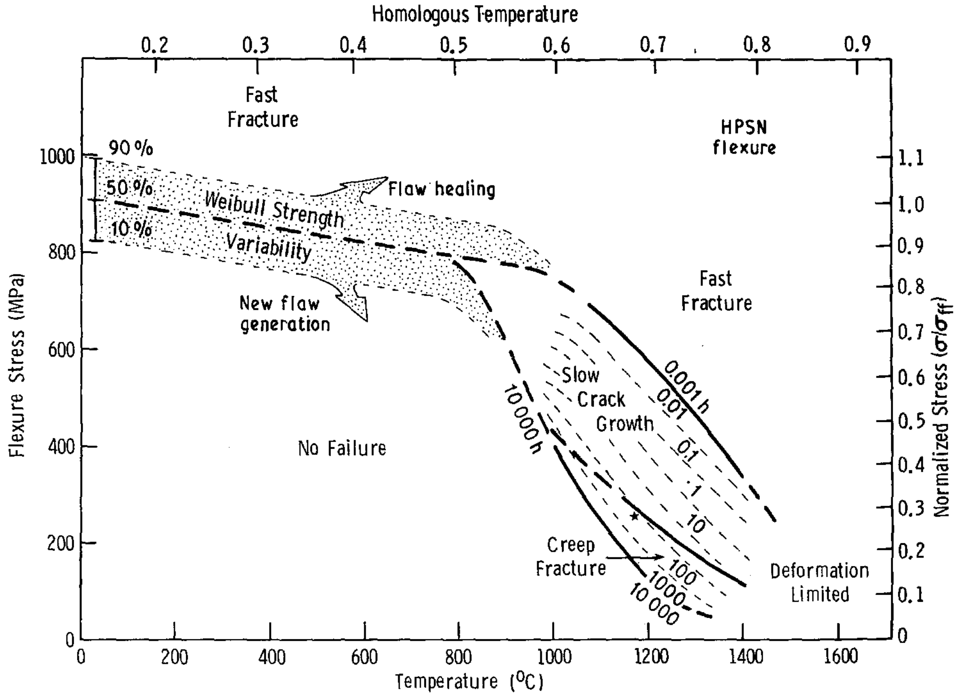

Figure 12 Comprehensive fracture map for MgO-doped HPSN tested in flexure in air. The star shows the conditions used by Tighe and Wiederhorn [55] for their strength degradation map. σ_{ff} is the fast fracture stress.

The effective volume of Govila's tension specimens is approximately equal to the volume in the gauge length and was 154 mm^3. The effective volume of the flexure specimens is

$$V_{\mathrm{E,flex.}} = V[(m + 2)/4(m + 1)^2] \qquad (5)$$

which ranged from 3.3 to 4.8 mm^3 for the flexure specimens used in this study. The equation then suggests the ratio of flexure strength to tension strength is 1.2 to 1.3. This, coincidentally, is in good agreement with the ratio of 1.35 reported by Ohji [66] for HPSN at room temperature and 1200° C for a different HPSN tested both in tension and flexure. The present ratio is somewhat less than the estimated 1.6 to 1.7 experimental ratio observed at 1000° C for specimens with failure times greater than 0.1 h (Table II). The difference could easily be accounted for by the onset of limited creep relaxation in the flexure specimens, differences in the specimen preparation of billet sources, or any one of the assumptions in the Weibull size analysis. (A two parameter Weibull function is assumed with volume flaws. The same class flaws are assumed to be responsible for failure in each specimen type. It is often difficult to determine the original natural flaw origin when significant slow crack growth has occurred. The pertinent flaws to compare at the high-temperature stress rupture conditions could very well be volume flaws as proven in [17] for flexure tests. Govila [40, 41] showed very convincingly that the SCG origins at 1000 and 1200° C were internal.) One significant experimental error with the flexure specimens is the friction constraint due to fixed points of loading [67]. The friction error is well known in room-temperature fixtures, and is typically causes stresses in the specimens to be reduced by 5% to 15% from what is computed from simple beam theory [67]. Very little has been reported at elevated temperatures, but preliminary experiments at MTL with the same HPSN used in this study indicate the error is of the order of 10% for stress rupture specimens at 1200° C over all times from loading to 100 h. Thus the stress correction for flexure to tensile stress becomes 1.3 × 1.1 = 1.4 which is in better agreement with the observed results at 1000° C.

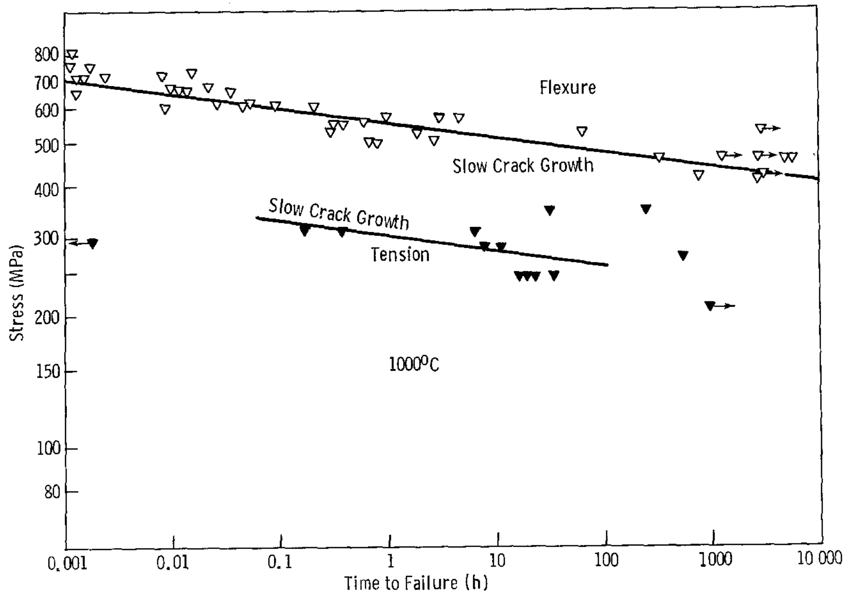

Figure 13 Tensile [40, 41] and flexural (this report) stress rupture data for HPSN at 1000° C in air.

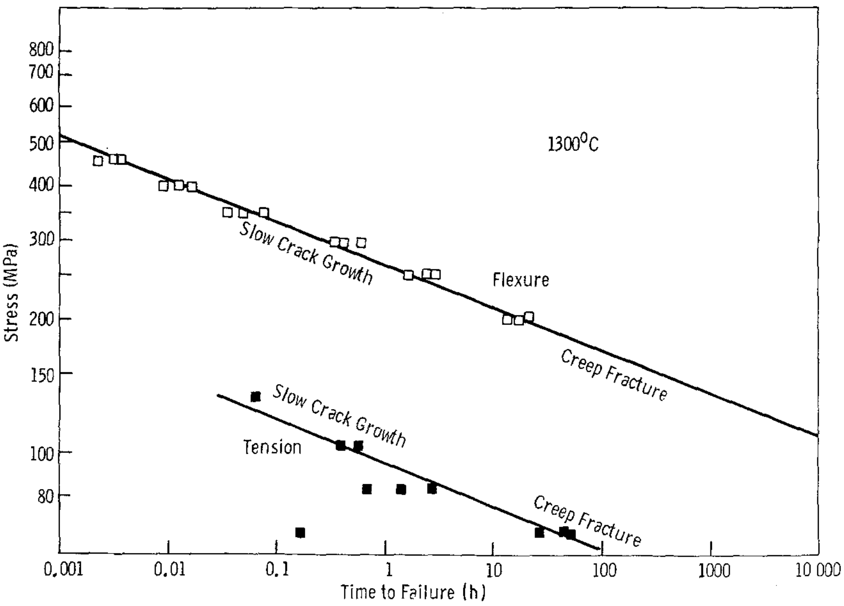

Figure 14 Tensile [40, 41] and flexural (this report) stress rupture data for HPSN in air.

Relaxation of the tensile stresses will occur in specimens at higher temperatures where creep occurs. The great difficulty of properly interpreting flexural creep data has been discussed previously. For the present purposes, we wish to consider steady state phenomena (in the 1 to 100 h range by which time much of the primary creep has diminished) and use the conventional constitutive equation

$$\dot{\varepsilon}_{ss} = B\sigma_a^n \exp(-Q_c/RT) \qquad (6)$$

where $\dot{\varepsilon}_{ss}$ is the steady state creep rate, B and n are constants and Q_c is the activation energy for creep. This relationship has been shown to be suitable with a stress exponent n of 2.0 by a number of investigators [25, 45, 47, 68, 69]. An important and necessary adjustment to this constitutive relationship is to note creep rates in tension are appreciably higher than those in compression for the same stress and temperature. Fortunately, Seltzer [52] has shown that for this HPSN the activation energy and stress exponents are the same in tension and compression, and the difference in creep rates is a simple proportionality constant. While many authors have cited ratios of tension to compression creep rates for HPSN in the literature (for example [20, 24]), there appears to be only three specific original experiments to actually measure the phenomena as shown in Table III. Talty and Dirks [69] used trapezoidal shaped flexure specimens to intentionally measure the different creep rates. Seltzer [52] combined data from several sources including his own tensile and compression work and got ratios of 4.7 or 9.3 depending upon whether HS 130 or NC 132 data was used. The exact ratio is a consequence of the grain-boundary phase composition and chemistry as noted by Lange [45]. It is especially interesting to observe Seltzer's work was over a broad temperature range: 1200 to 1400° C. Kossowsky *et al.* [47] mention a single experiment at 1370° C where 689 MPa compressive stress was required to achieve the same creep rate for a tensile specimen at 69 MPa. This compression to tension stress ratio of 10 can be converted to an equivalent creep rate of 100 times faster in tension than compression if the stress exponent is 2. This is only one experiment (albeit a much cited one) and it is felt that the compressive specimen probably was loaded in a stress regime wherein there may have been a higher creep exponent (4+) as shown in [25, 47]. It thus seems reasonable to rely upon the results of the more comprehensive former studies and use

$$\dot{\varepsilon}_t = (5 \text{ to } 9) \times \dot{\varepsilon}_c \qquad (7)$$

Two analyses have been done for the case of steady state creep modelled by Equation 6 with different constants B for tension and compression [20, 23]. (Grathwohl's analysis [20] is in terms of S, the ratio of compressive to tension stresses to get the same creep rates. The ratios of creep rates cited above can readily be converted to an S factor by noting the stress exponent n is 2 in Equation 6.) The stress for steady state conditions in the flexure specimen is reduced by a factor of 1.5 to 1.6 depending upon whether a creep rate ratio of 5 to 9 is used. Thus in summary, combining the correction factors for adjusting flexure to tension at 1200° C or higher:

$$\sigma_f = (1.3) \times (1.1) \times (1.5 \text{ to } 1.6) \times \sigma_t = 2.1 \text{ to } 2.3\sigma_t \qquad (8)$$

TABLE III Ratio of tensile to compressive creep rates in HPSN

Method	Temperature–stress		Ratio	Reference
	°C	(MPa)		
Tapered flexure specimens	1250–1300	66–156	5.6	Talty and Dirks [69]
Tension and compression	1200–1400	68	4.7–9.3	Seltzer [52]
Tension and compression	1370	68	100	Kossowsky, *et al.* [47]

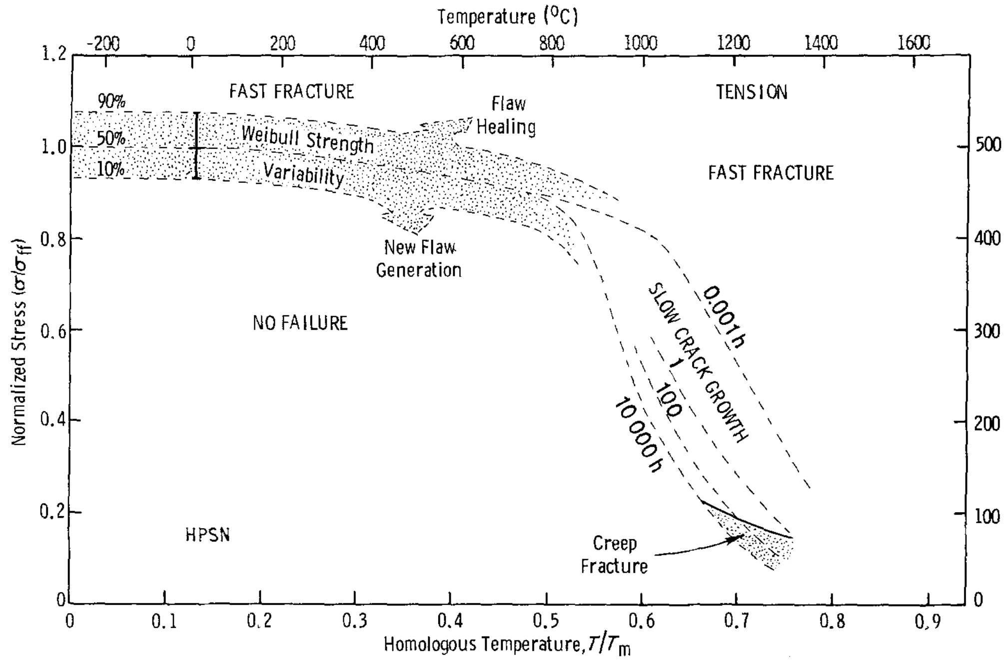

Figure 15 Fracture map for MgO-doped HPSN in air in direct tension.

which although not in complete agreement with the experimentally observed shifts of 2.6 to 2.8, is qualitatively correct.

Fig. 15 is a fracture map for direct tension loading for this grade HPSN. The overall form and the fields are in accordance with the flexure fracture map (Fig. 12), but available tension data from the literature were used to set the stress and temperature values. The homologous temperature axis has been extended to 0 and the inert strength is assumed to be the same as the fast fracture strength at room temperature because no known static fatigue phenomena are active at such low temperatures for HPSN. The band separating the fast fracture and no failure zones at low temperature is again depicted by a shaded zone with 10%, 50% and 90% Weibull failure probabilities. A shallow trend of diminishing strength is shown as reported previously [40, 43, 44]. The median fast fracture line then splits into median lines of constant failure time in the zone where slow crack growth becomes operative ($T >$ 900° C). The loci of failure time are empirical results from the work of Govila [40, 41]. These lines have much less certainty that the flexure loci because the tension results had much higher scatter. Govila unfortunately did not report fast fracture or inert tension strength results to compliment his superb stress rupture data. An inert strength can be estimated from extrapolating his 1000° C tension stress rupture results back to 0.001 h (Fig. 13) at the same slope as the flexure results. (Creep deformation in the flexure data is negligible at this temperature [25] and the elastic flexure stresses are probably not relaxed.) This estimated tension fast fracture strength at 1000° C is then adjusted by the amount of strength degradation that occurs from room temperature to 1000° C which is approximately 11% from [40, 43, 44] and the flexure results of this study. The fast fracture room-temperature tension strength is thus estimated to be 500 MPa. Of course this should be evaluated for each batch of material and each given specimen size because Weibull size effects will influence this value.

The fracture maps (Figs 12 and 15) integrate and reconcile the static fatigue results of all previous MgO-doped HPSN studies. Batch to batch material variations lead to fast fracture variability of about 20%, and times-to-failure vary by a factor of 10, but otherwise results are in excellent agreement. The comprehensive tension creep and stress rupture data of Kossowsky *et al.* [47] on the HS-130 grade was primarily in the low-stress high-temperature creep fracture field. Their work conclusively demonstrated that a Monkman Grant relationship (Table I) describes lifetime over a wide temperature range (1150 to 1315° C) with failure times from 20 to 1920 h. The more recent tension work by Govila on NC 132 was at higher stresses and primarily led to slow crack growth failures.

The strength degradation map of Tighe and Wiederhorn [55] would correspond to one single point on the flexure fracture map (Fig. 12) at 250 MPa and 1200° C. Their map shows a detailed evolution of retained fast fracture strength, for stress rupture specimens loaded at that one condition. Over 100 flexure specimens were loaded at this condition. At regular intervals, several were broken to determine the fast fracture strength. After an initial strengthening due to healing of machining damage, strength began to degrade due to the creation of new defects (pits on the surface). Ultimately creep cavitation occurred leading to fracture at times over 500 h, with a median failure time of about 1500 h. The fracture maps of this study (Figs 9 and 12) show creep fracture is indeed the cause of fracture but with failure times about 200 h, a difference likely due to material variability.

An alternative procedure of stress rupture testing, interrupted static fatigue, has been advocated by Minford and Tressler [70] for silicon carbide, and later by Foley and Tressler [71] for sintered silicon nitride. Stress rupture specimens are loaded at a variety of stresses and temperatures. At the same elapsed time (10 or 100 h) all experiments are stopped, and the fast fracture strength is measured. It is possible to determine a stress corrosion limit (or threshold stress intensity factor) below which no time-dependent failure will occur. The method was not applied to an MgO-doped HPSN, but in principle it would define the lower boundary between the "no failure" and "creep fracture" or "slow crack growth" regimes on the fracture maps.

The latter studies raise the issue of whether the more fundamental driving force for fracture is stress or stress intensity. Which should be used as the vertical axis on the fracture maps? As shown in Table I, stress intensity does control both fast fracture and slow crack growth. Determination of stress intensity in a loaded component is difficult, however, due to uncertainties in the flaws and particularly their severity (factor Y in Table I). Stress intensity is irrelevant in the creep fracture regime and stress is the more fundamental parameter. Johnson *et al.* [3] have similarly noted the shortcomings of the use of stress intensity for materials under creep fracture conditons. Thus it would seem that stress is an adequate parameter to characterize the driving force for fracture. Its usage on ceramic fracture maps will make the maps consistent with the deformation and fracture maps already in use for metallic and polymeric materials.

Although in principle the fracture mechanism map can be theoretically derived, it was empirically developed in the present study. The slow crack growth creep fracture regimes are identifiable by comparisons of times-to-failure of artificially flawed compared to as-machined specimens. This approach must be used with extreme caution on other materials, however, because it can strongly bias results towards slow crack growth as the mechanism of failure. For example, it was shown in a stress rupture study on sintered silicon carbide that the use of artificially flawed specimens completely masked the presence of stress corrosion, static fatigue phenomenon involving surface connected pores [72]. Johnson *et al.* [3] also reported that Knoop-induced flaws grew differently than natural defects in an alumina. Fractography is a key tool for fracture map development. Other studies have noted that changes in slope on stress rupture graphs [11, 58] or changes in creep strains to fracture [58] can distinguish different regimes of static fatigue phenomena.

Matsui *et al.* [73] created a hypothetical fracture map for two sintered silicon nitrides and superimposed the operating conditions of a ceramic turbocharger to illustrate a designer's approach to the use of such maps. Their maps illustrated slow crack growth, creep strain and oxidation limiting conditions.

Fracture maps are probably better derived from stress rupture experiments rather than fracture mechanics tests. The latter have been disappointing in many instances (especially at high temperature, and particularly with HPSN) in their ability to correlate to stress rupture data on laboratory specimens [17, 74, 75] or components [76]. (The work in [75] is one of the few successful instances.) Large crack fracture mechanics test results are irrelevant or useless in many instances such as for predicting creep fracture or surface stress corrosion attack of pores or microporous zones in advanced ceramics.

How much testing is necessary to devise a fracture map? This will depend upon the material. Over 500 flexure specimens were needed to create the comprehensive HPSN maps. This is partially a consequence of the statistical nature of strength of ceramics. Several dozen complimentary tension results were critical in extending the utility of the map to more generalized loading. Future stress rupture studies should feature judicious and complimentary flexure and tension stress rupture experimentation. The companion paper [11] develops a fracture map for a more contemporary silicon nitride but with far fewer specimens.

6. Conclusions

The fracture map combines all of the mechanisms that limit the strength of a ceramic and puts them into perspective. Two mechanisms of static fatigue at elevated temperature exist in HPSN: creep fracture and slow crack growth. Both are related to the deformation of the intergranular second phase. The difference is a matter of scale. Creep deformations in the slow crack growth regime are confined to the immediate vicinity of a crack tip and lead to crack extension. Bulk deformation will alternatively lead to creep fracture. Several empirical approaches were used to develop the fracture maps. Fracture mechanism maps can be appreciated by and can guide the work of both the engineering and materials science communities.

References

1. G. D. QUINN, *Ceram. Eng. Sci. Proc.* **3** (1–2) (1982) 77.
2. S. M. WIEDERHORN, B. J. HOCKEY, R. F. KRAUSE and K. JAKUS, *J. Mater. Sci.* **21** (1986) 810.
3. S. M. JOHNSON, B. J. DALGLEISH and A. G. EVANS, *J. Amer. Ceram. Soc.* **67** (1984) 759.
4. W. BLUEMENTHAL and A. G. EVANS, *ibid.* **67** (1984) 751.
5. T. OKADA and G. SINES, *ibid.* **66** (1983) 719.
6. A. G. ROBERTSON and D. S. WILKINSON, in "Fracture Mechanics of Ceramics", Vol. 7, edited by R. C. Bradt, A. G. Evans, D. P. H. Hasselman and F. Lange (Plenum, New York, 1986) p. 311.
7. D. P. H. HASSELMAN, A. VENKATESWAREN and C. SHIH, in "Surfaces and Interfaces in Ceramic and Ceramic Metal Systems", Materials Science Research, Vol. 14, edited by J. Pask and E. Evans (Plenum, New York, 1981) p. 323.
8. P. J. WRAY, *J. Appl. Phys.* **40** (1969) 4018.
9. R. J. FIELDS, T. WEERASOORIYA and M. F. ASHBY, *Met. Trans.* **11A** (1980) 333.
10. C. GANDHI and M. ASHBY, *Acta Metall.* **27** (1979) 1565.
11. G. D. QUINN and W. R. BRAUE, *J. Mater. Sci.* **25** (1990).
12. G. D. QUINN, in "Methods for Assessing the Structural Reliability of Brittle Materials", ASTM STP 844, edited by Freiman and C. Hudson (American Society of Testing and Materials, Philadelphia, Pennsylvania, 1984) p. 177.
13. *Idem, Ceram. Engng Sci. Proc.* **5** (1984) 596.
14. *Idem*, in "Fracture Mechanics of Ceramics", Vol. 8, edited by R. Bradt, A. Evans, D. Hasselman and F. Lange (Plenum, New York, 1986) p. 319.
15. M. L. TORTI, in "Ceramics for High Performance Applications III, Reliability", edited by E. Lenoe, R. Katz and J. Burke (Plenum, New York, 1983) p. 261.

16. G. D. QUINN, in "Ceramic Materials and Components for Engines", edited by W. Bunk and H. Hausner (Deutsche Keramische Gessellschaft, Berlin, 1986) p. 931.
17. G. D. QUINN and J. B. QUINN, in "Fracture Mechanics of Ceramics", Vol. 6, edited by R. Bradt, A. Evans, D. Hasselman and F. Lange (Plenum, New York, 1983) p. 603.
18. G. D. QUINN, "Characterization of Turbine Ceramics After Long-Term Environmental Exposure", US Army AMMRC Technical Report TR80-15 (Army Materials Technology Laboratory, Watertown, Massachusetts, 1980).
19. *Idem*, "Guide to the Construction of A Simple 1500 C Test Furnace", US Army AMMRC Technical Report TN 77-4, August 1977 (Army Materials Technology Laboratory, Watertown, Massachusetts, republished as TR 83-1, January 1983).
20. H. COHRT, G. GRATHWOHL and F. THÜMMLER, *Res. Mech. Lett.* **1** (1981) 159.
21. G. GRATHWOHL, in "Deformation of Ceramic Materials II", edited by R. Tressler and R. Bradt (Plenum, New York, 1984) p. 573.
22. T. FETT, *J. Mater. Sci. Lett.* **6** (1987) 967.
23. T. FETT and D. MUNZ, *Int. J. High Tech. Ceram.* **4** (1988) 281.
24. T. FETT, K. KELLER and D. MUNZ, *J. Mater. Sci.* **23** (1988) 467.
25. R. ARONS and J. TIEN, *ibid.* **15** (1980) 2046.
26. D. F. CARROLL, T. J. CHUANG and S. M. WIEDERHORN, *Ceram. Engng Sci. Proc.* **9** (1988) 635.
27. D. S. WILKINSON, *J. Amer. Ceram. Soc.* **71** (1988) 562.
28. G. DAS, M. G. MENDIRATTA and G. R. CORNISH, *J. Mater. Sci.* **17** (1982) 2486.
29. G. GRATHWOHL and F. THÜMMLER, *ibid.* **13** (1978) 1177.
30. A. VENKATESWAREN and D. P. H. HASSELMAN, *ibid.* **16** (1981) 1627.
31. A. R. ROSENFIELD, W. H. DUCKWORTH and D. K. SHETTY, *J. Amer. Ceram. Soc.* **68** (1985) 485.
32. K. JAKUS and S. WIEDERHORN, *ibid.* **71** (1988) 832.
33. S. WIEDERHORN, L. CHUCK, E. FULLER and J. TIGHE, in "Tailoring of Multiphase and Composite Ceramics", Materials Science Research, Vol. 20, edited by R. E. Tressler, G. L. Mecholsky, C. G. Pantano and R. E. Newnham (Plenum, New York, 1986) p. 755.
34. R. J. CHARLES, *J. Appl. Phys.* **29** (1958) 1657.
35. A. G. EVANS, L. R. RUSSELL and D. W. RICHERSON, *Met Trans.* **6A** (1975) 707.
36. R. DAVIDGE, J. McLAREN and G. TAPPIN, *J. Mater. Sci.* **8** (1973) 1699.
37. J. RITTER Jr, in "Fracture Mechanics of Ceramics 4", edited by R. Bradt, D. Hasselman and F. Lange (Plenum, New York, 1978) p. 667.
38. G. D. QUINN and L. SWANK, *Commun. Amer. Ceram. Soc.*, January (1983) C31.
39. G. TRANTINA, *J. Amer. Ceram. Soc.* **62** (1979) 377.
40. R. GOVILA, "Ceramic Life Prediction Parameters", US Army Technical Report, TR 80-18 (US Army Materials Technology Laboratory, Watertown, Massachusetts, May 1980).
41. *Idem, J. Amer. Ceram. Soc.* **65** (1982) 15.
42. N. TIGHE and S. WIEDERHORN, in "Fracture Mechanics of Ceramics", Vol. 6, p. 403.
43. R. BRATTON and D. MILLER, in "Ceramics for High Performance Applications II", edited by J. Burke, E. Lenoe and R. Katz (Brook Hill, Chestnut Hill, Massachusetts, 1978) p. 689.
44. D. MILLER, C. ANDERSON, S. SINGHAL, F. LANGE, E. DIAZ, R. KOSSOWSKY and R. BRATTON, "Brittle Materials Design, High Temperature Gas Turbine Material Technology, Final Report", CTR 76-32 Vol. 4 (US Army Materials and Mechanics Research Center, Dec. (1976).
45. F. F. LANGE, *Int. Met. Rev.* **7** (1980) 1.
46. N. J. TIGHE, *J. Mater. Sci.* **13** (1978) 1455.
47. R. KOSSOWSKY, D. MILLER and E. DIAZ, *ibid.* **10** (1975) 983.
48. N. J. TIGHE, S. M. WIEDERHORN, T. J. CHUANG and C. L. MCDANIEL, "Deformation in Ceramic Materials II", edited by R. Tressler and R. Bradt (Plenum, New York, 1984) p. 587.
49. K. JAKUS, J. R. RITTER Jr and J. P. FAHEY, *Commun. Amer. Ceram. Soc.*, September (1982) C143.
50. S. UD DIN and P. NICHOLSON, *J. Mater. Sci.* **10** (1975) 1375.
51. D. R. MOSHER, R. RAJ and R. KOSSOWSKY, *J. Mater. Sci.* **11** (1976) 49.
52. M. SELTZER, *Amer. Ceram. Soc. Bull.* **56** (1977) 418.
53. W. WEIBULL, *J. Appl. Mech.* **18** (1951) 293.
54. D. G. S. DAVIES, *Proc. Brit. Ceram. Soc.* **22** (1973) 429.
55. N. J. TIGHE and S. M. WIEDERHORN, in "Fracture Mechanics of Ceramics", Vol. 5, edited by R. Bradt, A. Evans, D. Hasselman and F. Lange (Plenum, New York, 1983) p. 403.
56. F. C. MONKMAN and N. J. GRANT, *Proc. ASTM* **56** (1956) 593.
57. G. GRATHWOHL, *Int. J. High Tech. Ceram.* **4** 123 (2) (1988).
58. U. ERNSTBERGER, G. GRATHWOHL and F. THÜMMLER, in "Ceramic Materials and Components for Engines", edited by W. Bunk and H. Hausner (Deutsche Keramische Gesselschaft, Berlin, 1986) p. 485.
59. G. GRATHWOHL, in "Creep and Fracture of Engineering Materials and Structures", edited by B. Wilshire and D. Owen (Pineridge Press, Swansea, UK, 1984) p. 565.
60. F. F. LANGE and B. I. DAVIS, *Bull. Amer. Ceram. Soc.* **59** (1980) 827.
61. F. F. LANGE, B. I. DAVIS and M. G. METCALF, *J. Mater. Sci.* **18** (1983) 1497.
62. K. JAKUS, J. RITTER Jr and W. P. ROGERS, *J. Amer. Ceram. Soc.* **67** (1984) 471.
63. E. M. LENOE, unpublished results.
64. G. QUINN and G. WIRTH, "Biaxial Static Fatigue of Silicon Nitride", in "Ceramic Materials and Components for Engines", edited by V. Tennery (Am. Ceram. Soc., Westerville, Ohio, 1989) p. 824.
65. G. QUINN and G. WIRTH, *Mater. Sci. Engng* **A109** (1989) 147.
66. T. OHJI, *Int. J. High Tech. Ceram.* **4** (1988) 211.
67. F. I. BARATTA, G. D. QUINN and W. T. MATTHEWS, "Errors Associated with Flexure Testing of Brittle Materials", US Army MTL Technical Report, TR 87-35, July 1987.
68. G. W. HOLLENBERG, G. R. TERWILLIGER and R. S. GORDON, *J. Amer. Ceram. Soc.* **54** (1971) 196.
69. P. K. TALTY and R. A. DIRKS, *J. Mater. Sci.* **13** (1978) 580.
70. E. J. MINFORD and R. E. TRESSLER, *J. Amer. Ceram. Soc.* **66** (1983) 338.
71. M. R. FOLEY and R. E. TRESSLER, *Adv. Ceram. Mater.* **3** (1981) 382.
72. G. D. QUINN and R. N. KATZ, *J. Amer. Ceram. Soc.* **63** (1980) 117.
73. M. MATSUI, Y. ISHIDA, T. SOMA and I. ODA, in "Ceramic Materials and Components for Engines", edited by W. Bunk and H. Hausner (Deutsche Keramische Gesselschaft, Berlin, 1986) p. 1043.
74. B. PLETKA and S. WIEDERHORN, *J. Mater. Sci.* **22** (1987) 1247.
75. G. D. QUINN, *ibid.* **22** (1987) 2309.
76. R. R. BAKER, L. R. SWANK and J. C. CAVERLY, "Ceramic Life Prediction Methodology – Hot Spin Disc Life Program", US Army Materials and Mechanics Research Center, Technical Report TR 83-44, August 1983.

Received 24 July
and accepted 26 September 1989